Research Article

Rachid Chebbi*

An analytical model for solute transport from blood to tissue

https://doi.org/10.1515/phys-2022-0026
received November 24, 2021; accepted March 28, 2022

Abstract: For narrow tubes, red blood cells concentrate in the core region, leaving an annular zone called cell-free layer. This has an impact on both the tube hematocrit level (Fåhraeus effect) and the apparent blood viscosity (Fåhraeus–Lindqvist effect). Blood flow, mass transfer across the microvessel membrane, and diffusion in the tissue affect the solute concentration profiles. The Krogh tissue cylinder concept, limiting mass transfer to a cylinder around each microvessel, and the marginal zone concept (introduced by Haynes to analyze blood flow dynamics in narrow tubes) are both used to develop a model for solute transfer from blood in microvessels to the surrounding tissues, based on fundamentals. The analysis accounts for advection and diffusion in each zone of the microvessel, solute transport in the microvessel membranes, and diffusion and reaction in the tissues. The present investigation provides an analytical solution. The approach can be extended to treat other kinetic models, while accounting for Fåhraeus and Fåhraeus–Lindqvist effects in blood microvessels. The model is validated against published results for glucose transport from blood to tissue.

Keywords: mass transfer, blood flow, tissue, Krogh cylinder, marginal zone theory

1 Introduction

Transport of a solute from blood to the surrounding tissues involves transport in the microvessel, through the microvessel wall, and transport in the tissue. Blood flow in the microvessels affects the concentration profiles. For small blood vessels below 500 μm diameter, diameter affects both the tube hematocrit (Fåhraeus effect) and the apparent blood viscosity (Fåhraeus–Lindqvist effect) with red blood cells (RBCs) concentrating in the core region [1–8]. Haynes marginal zone theory considers blood as consisting of two layers: a marginal zone (cell-free layer) surrounding a core region where RBCs concentrate [7]. Both zones are treated as continuum fluids. The theory was used to investigate Fåhraeus and Fåhraeus–Lindqvist effects [9–11]. Other blood flow models include shear-induced models [12–15] using the shear-induced particle migration concept [16,17] and elastic stress-induced models [18–22]. Non Newtonian and viscoelastic models for blood are reviewed in Arciero *et al.* [23] and in the references therein. Mesoscale models account for the particulate aspect of blood [23,24].

The Krogh cylinder model was introduced by Krogh to solve for transport of oxygen in tissue [25]. The assumptions used and extensions of the model are discussed in studies [23,26–28] and the references therein. In the case of oxygen transport, accounting for enhanced oxygen transport by myoglobin and reaction in RBCs is required [26,28]. Different geometries for RBCs were proposed [28]. An analytical solution, assuming cylindrical RBCs to occupy the lumen of the blood vessel shows the intra-capillary high resistance to oxygen transport [29]. Groebe [30] accounted for axisymmetric diffusion of oxygen through three layers assuming cylindrical RBCs with plasma filling the gap between them. An analytical solution and a discussion of the simplifying assumptions are provided in ref. [30]. Blood is assumed to be formed by spherical RBCs, in line, equidistant, and surrounded by plasma in ref. [31]. A frame of reference moving with the RBCs is selected [31]. Other shapes for RBCs were selected and assumed to be surrounded by plasma: cylindrical (using a frame of reference in which RBCs are fixed) [32] and parachute form [33,34] (with a reference system in which RBCs are fixed in ref. [33], while considering RBCs motion in the frame of reference in the study [34]). Transport of other species like NO in relation with oxygen transport are discussed in refs. [23,27,28,30]. A model for biofluids flow in slowly and successively contracting and expanding rectangular geometry with two weakly permeable walls (allowing for flow through the walls) is solved using the homotopy method [35].

* **Corresponding author: Rachid Chebbi,** Department of Chemical Engineering, American University of Sharjah, Sharjah, United Arab Emirates, e-mail: rchebbi@aus.edu, fax: +971-6 515 2979

Open Access. © 2022 Rachid Chebbi, published by De Gruyter. This work is licensed under the Creative Commons Attribution 4.0 International License.

A model for solute transfer accounting for advection and diffusion using Krogh model for transport in tissue is presented in Fournier [3]. For intra-capillary transport, blood velocity is assumed uniform inside the capillary and an overall transport coefficient from blood to the outer surface of the capillary wall (external side of the capillary membrane) is used in the final expressions for solute concentration in ref. [3].

The present model uses Krogh concept for solute transport in the tissue [25] (with mass transfer limited to a cylinder around each microvessel) along with Haynes marginal zone concept for blood flow [7] (considering the microvessel as formed of a cell-free layer and a core region where RBCs concentrate). The model for solute transport from blood to the surrounding tissue accounts for advection and diffusion in both the core region and the cell-free layer in the microvessel, solute transport in the microvessel membrane, and diffusion and reaction in the tissue (Figure 1). The approach is based on the fundamentals of fluid mechanics and mass transfer, where the velocity profiles in the two zones, core and cell-free layer, are considered to account for advection in the mass transfer equations. An analytical approach combining the different steps in solute transport is provided.

2 Governing equations

Haynes theory considers blood as consisting of two phases: an annular cell-free layer and a core layer containing RBCs. The velocity profile is discussed in Fournier [3], Chebbi [11], and the references therein. Only boundary conditions and related results of the present work are presented here. A schematic diagram of a microvessel and its Krogh cylinder is shown in Figure 1. The cylindrical coordinates r and z are used.

For fully developed flow, the velocity profile is independent of z. The following boundary conditions express continuity of the velocity and shear stress at the two zones interface $r = r_i$, in addition to finite shear stress at the axis of the microvessel and no-slip boundary condition at the inner surface of the microvessel wall

$$\text{at } r = r_i, \quad v_c = v_a, \tag{1}$$

$$\text{at } r = r_i, \quad \mu_c \frac{dv_c}{dr} = \mu_a \frac{dv_a}{dr}, \tag{2}$$

$$\text{at } r = 0, \ \mu_c \frac{dv_c}{dr} \text{ is finite}, \tag{3}$$

$$\text{at } r = R, \quad v_a = 0. \tag{4}$$

Applying the momentum balance for the two zones yields

$$-\mu_c \frac{dv_c}{dr} = -\mu_a \frac{dv_a}{dr} = p_G \frac{r}{2}, \tag{5}$$

where v denotes velocity, μ represents viscosity, r is the radial coordinate, R is the microvessel radius, p_{gr} is the absolute value of the pressure gradient, and subscripts a, c, and i denote the annular region, the core region, and the two-zone interfacial area, respectively.

The velocity profiles in the core region and the cell-free layer (annular region) are given by

$$v_c = A_c(r^2 - r_i^2) + v_i; \quad v_i = A_a(r_i^2 - R^2), \tag{6}$$

$$v_a = A_a(r^2 - R^2), \tag{7}$$

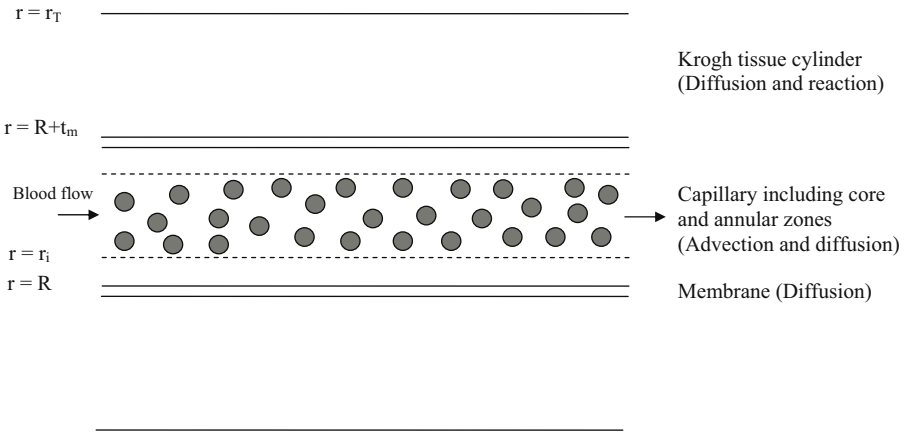

Figure 1: Schematic of a microvessel and its Krogh tissue cylinder showing the two zones introduced in Haynes' model: cell-free layer surrounding a core zone assumed of uniform RBCs concentration.

where

$$A_c = \frac{-P_{gr}}{4\ \mu_c}; \quad A_a = \frac{-P_{gr}}{4\ \mu_a}. \tag{8}$$

The average velocity v^* is given by

$$Q = v^*\pi R^2 = \frac{\pi P_{gr}}{8}\left[\frac{r_i^4}{\mu_c} + \frac{R^4 - r_i^4}{\mu_a}\right], \tag{9}$$

where Q is the blood volumetric flow rate.

The core hematocrit H_C is assumed uniform. The conservation of hematocrit yields the following relations [3,11]:

$$\frac{H_T}{H_D} = \sigma^2\left[1 + \frac{(1-\sigma^2)^2}{\sigma^2\left(2 - 2\sigma^2 + \sigma^2\frac{\mu_a}{\mu_c}\right)}\right]; \quad \frac{H_T}{H_C} = \sigma^2, \tag{10}$$

where H_T is the tube hematocrit, H_D is the discharge hematocrit, and $\sigma = r_i/R$.

The apparent viscosity μ_{app} is given by the Hagen–Poiseuille equation and is related to the core zone viscosity by:

$$\frac{\mu_a}{\mu_{app}} = 1 + \sigma^4\left[\frac{\mu_a}{\mu_c} - 1\right]; \quad \mu_{app} = \frac{\pi P_{gr} R^4}{8Q}. \tag{11}$$

The core zone viscosity is assumed to be a function of H_C (up to 0.6) according to ref. [3]:

$$\frac{\mu_a}{\mu_c} = 1 - \alpha H_C, \tag{12}$$

where

$$\alpha = 0.070\ \exp\left[2.49H_C + \frac{1{,}107}{T}\exp(-1.69\ H_C)\right], \tag{13}$$

and T is blood temperature in Kelvin.

The mass transfer model accounts for advection-diffusion in the microvessel side, mass transfer across the microvessel membrane, and diffusion and zero-order reaction in the surrounding tissues demarcated by the Krogh cylinder. For small concentrations and nearly constant temperature, the diffusion coefficients are constant, and the use of conservation of mass of solute yields the following partial differential equations assuming steady state (zero accumulation term):

$$v_c\frac{\partial c_c}{\partial z} = D_c\left[\frac{1}{r}\frac{\partial}{\partial r}\left(r\frac{\partial c_c}{\partial r}\right) + \frac{\partial^2 c_c}{\partial z^2}\right], \tag{14}$$

$$v_a\frac{\partial c_a}{\partial z} = D_a\left[\frac{1}{r}\frac{\partial}{\partial r}\left(r\frac{\partial c_a}{\partial r}\right) + \frac{\partial^2 c_a}{\partial z^2}\right], \tag{15}$$

where z is the axial cylindrical coordinate, c denotes the solute concentration, D represents the diffusion coefficient of the solute, and subscripts c and a refer to the core and annular zones, respectively. The effective diffusion coefficient is used for the core region as it consists of plasma and RBCs. In the case of oxygen transport for instance, a reaction term involving the solute consumption needs to be accounted for in the solute mass balance. The present model does not include the case where reaction involving the solute occurs in the blood side.

The following boundary conditions express continuity of concentration and fluxes at the interface between the core and annular zones, in addition to finite concentration gradient at the centerline:

$$\text{at } r = r_i, \quad c_c = c_a, \tag{16}$$

$$\text{at } r = r_i, \quad D_c\frac{\partial c_c}{\partial r} = D_a\frac{\partial c_a}{\partial r}, \tag{17}$$

$$\text{at } r = 0, \quad \frac{\partial c_c}{\partial r} \text{ is finite.} \tag{18}$$

The effective diffusion coefficient D_c can be obtained using Maxwell equation [3,36]:

$$D_c = \frac{2D_a + D_{RBC} - 2H_c(D_a - D_{RBC})}{2D_a + D_{RBC} + H_c(D_a - D_{RBC})}, \tag{19}$$

where D_{RBC} is the solute diffusion coefficient in RBCs. Mass transfer through the microvessel membrane is mainly due to diffusion, with negligible transport by filtration [3]. Mass transfer in the membrane is considered in the present model as purely diffusional, and the boundary condition at the microvessel wall can be written at the inner side of the membrane as [3]:

$$\text{at } r = R, \ -D_a\frac{\partial c_a}{\partial r} = P_M(c_a - c_T|_{r=R+t_m}), \tag{20}$$

and as

$$\text{at } r = R + t_m, \quad -D_T\frac{\partial c_T}{\partial r} = P_M(c_a - c_T|_{r=R+t_m})\frac{R + t_m}{R}, \tag{21}$$

at the outer side of the microvessel membrane, where subscript T refers to the tissue, and P_M and t_m denote the solute permeability and membrane thickness, respectively.

At the limit of the Krogh tissue cylinder, $r = r_T$, we have [3]:

$$\text{at } r = r_T, \quad \frac{\partial c_T}{\partial r} = 0, \tag{22}$$

which restricts mass transfer to the Krogh tissue cylinder surrounding the specific microvessel. This condition prevents mass transfer between the different Krogh cylinders.

In case the critical length L_{cr}, at which the solute concentration is zero, is larger than the microvessel length, then at the Krogh radius r_T, Eq. (22) is still valid,

but the reaction term in the model needs to be restricted to a smaller part of the Krogh cylinder where the solute is non zero.

In the tissue, we assume zero-order reaction occurring at a molar rate of R_0 per unit volume. Assuming constant D_T for the same arguments listed before for D_a and D_c, and using the constant density approximation, transport of solute can be easily shown to be governed by (Appendix B.11 [36]):

$$D_T\left[\frac{1}{r}\frac{\partial}{\partial r}\left(r\frac{\partial c_T}{\partial r}\right)+\frac{\partial^2 c_T}{\partial z^2}\right]-R_0=0. \tag{23}$$

Solving for c_T using boundary condition 22 gives [3]:

$$\begin{aligned} &c_T(r,z)-c_T(R+t_m,z)\\ &\quad=\Phi_T(r)-\Phi_T(R+t_m)\\ &\quad=\frac{R_0}{4D_T}[r^2-(R+t_m)^2]-\frac{R_0 r_T^2}{2D_T}\ln\left(\frac{r}{R+t_m}\right), \end{aligned} \tag{24}$$

where $\Phi_T(r)$ is the r-component of the solute concentration as defined in Eq. (25), in consistency with Krogh–Erlang solution [25,27].

In order to determine the concentration profile, an expression for $\Phi_T|_{R+t_m}$ is required.

3 Solution

Assuming sufficiently large Péclet number and large microvessel length, we neglect axial diffusion in the microvessel side and in its Krogh tissue cylinder. Excluding a small region near $z = 0$, we seek a solution of the form

$$\begin{aligned} &c_c=c_0+\Phi_c-b_c z;\quad c_a=c_0+\Phi_a-b_a z;\\ &c_T=c_0+\Phi_T-b_T z, \end{aligned} \tag{25}$$

where Φ_c, Φ_a, and Φ_T depend on r and are independent of z, c_0 is the average solute concentration in blood at $z = 0$, and b_a, b_c, and b_T are constants. A similar form of the solution with an r-component and a linear term proportional to z was used to treat the case of laminar fluid flow in a tube subject to a constant heat flux [36] (Chapter 10). The present case is different and accounts for two zones inside the microvessel, mass transfer across the membrane, and mass transfer and reaction in the surrounding Krogh cylinder. The results show that the solution is valid except very near the tube inlet [36] (Chapter 12).

The use of boundary conditions 16 and 20 yields $b_c = b_a = b_T = b$, with subscripts c, a, and T dropped, and b_c, b_a, and b_T simply denoted as b.

Substituting for velocities into Eqs. (14) and (15) while using Eqs. (6), (7), and (25) gives:

$$-b[A_c(r^2-r_i^2)+v_i]=D_c\frac{1}{r}\frac{d}{dr}\left(r\frac{d\Phi_c}{dr}\right), \tag{26}$$

$$-bA_a(r^2-R^2)=D_a\frac{1}{r}\frac{d}{dr}\left(r\frac{d\Phi_a}{dr}\right). \tag{27}$$

Boundary conditions (16)–(18) and (20) yield:

$$\text{at } r=r_i,\quad \Phi_c=\Phi_a, \tag{28a}$$

$$\text{at } r=r_i,\quad D_c\frac{d\Phi_c}{dr}=D_a\frac{d\Phi_a}{dr}, \tag{28b}$$

$$\text{at } r=0,\quad \frac{d\Phi_c}{dr}\text{ is finite}, \tag{29}$$

$$\text{at } r=R,\quad -D_a\frac{d\Phi_a}{dr}=P_M(\Phi_a-\Phi_T|_{r=R+t_m}). \tag{30}$$

Integrating Eqs. (26) and (27) while using Eq. (29) gives:

$$\begin{aligned} \Phi_c-\Phi_i=&-\frac{bA_c}{D_c}\left(\frac{r^4}{16}-r_i^2\frac{r^2}{4}+\frac{3}{16}r_i^4\right)\\ &-\frac{bv_i}{4D_c}(r^2-r_i^2), \end{aligned} \tag{31}$$

$$\Phi_a-\Phi_a|_{r=R}=-\frac{bA_a}{D_a}\left(\frac{r^4}{16}-R^2\frac{r^2}{4}+\frac{3R^4}{16}\right)+K\ln\frac{r}{R}, \tag{32}$$

where K is an integration constant.

In order to find b, a solute mass balance is made considering a control volume including the Krogh cylinder, the membrane, and blood limited to the interval $z - z + \Delta z$:

$$\begin{aligned} &\int_0^R 2\pi r v[(c_0+\Phi-bz)|_z-(c_0+\Phi-bz)|_{z+\Delta z}]dr\\ &\quad-\pi[r_T^2-(R+t_m)^2]\Delta z R_0=0. \end{aligned} \tag{33}$$

Φ is independent of z. Solving for b yields [3]:

$$b=\frac{\pi[r_T^2-(R+t_m)^2]R_0}{Q}. \tag{34}$$

Considering the Krogh cylinder as our selected control volume gives:

$$2\pi R\Delta z P_M(c_a|_{r=R}-c_T|_{r=R+t_m})-\pi[r_T^2-(R+t_m)^2]\Delta z R_0=0. \tag{35}$$

Rearranging the above equation yields

$$P_M(c_a|_{r=R}-c_T|_{r=R+t_m})=\frac{[r_T^2-(R+t_m)^2]R_0}{2R}. \tag{36}$$

Using Eq. (36) shows that the solute concentration profile, given by Eq. (24), is consistent with boundary condition (21).

Using the following definitions:

$$v^* = \frac{Q}{\pi R^2}; \quad A^* = \frac{v^*}{R^2}; \quad \Phi^* = \frac{bR^2 v^*}{D_a}. \tag{37}$$

The dimensionless variables are defined as

$$\begin{aligned} &\bar{r} = \frac{r}{R}; \quad \bar{v} = \frac{v}{v^*}; \quad \bar{A}_c = \frac{A_c}{A^*}; \quad \bar{A}_a = \frac{A_a}{A^*}; \\ &\overline{\Phi}_c = \frac{\Phi_c}{\Phi^*}; \quad \overline{\Phi}_a = \frac{\Phi_a}{\Phi^*}; \quad \bar{K} = \frac{K}{\Phi^*}. \end{aligned} \tag{38}$$

The dimensionless profiles are obtained using Eqs. (6), (7), (31), and (32).

$$\begin{aligned} &\bar{v}_c = \bar{A}_c(\bar{r}^2 - \sigma^2) + \bar{v}_i; \quad \bar{v}_a = \bar{A}_a(\bar{r}^2 - 1); \\ &\bar{v}_i = \bar{A}_a(\sigma^2 - 1), \end{aligned} \tag{39}$$

$$\begin{aligned} \overline{\Phi}_c - \overline{\Phi}_i = &-\frac{D_a}{D_c}\bar{A}_c\left(\frac{\bar{r}^4}{16} - \sigma^2\frac{\bar{r}^2}{4} + \frac{3}{16}\sigma^4\right) \\ &- \frac{D_a}{D_c}\frac{\bar{v}_i}{4}(\bar{r}^2 - \sigma^2), \end{aligned} \tag{40}$$

$$\overline{\Phi}_a - \overline{\Phi}_a|_{\bar{r}=1} = -\bar{A}_a\left(\frac{\bar{r}^4}{16} - \frac{\bar{r}^2}{4} + \frac{3}{16}\right) + \bar{K}\ln\bar{r}. \tag{41}$$

Converting Eqs. (8) and (9) to a dimensionless form gives:

$$\bar{A}_c = \frac{-2}{\sigma^4 + (1-\sigma^4)\frac{\mu_c}{\mu_a}}; \quad \bar{A}_a = \frac{-2}{(1-\sigma^4) + \sigma^4\frac{\mu_a}{\mu_c}}. \tag{42}$$

Using the relationship between concentrations across the microvessel membrane, Eq. (30), yields in a dimensionless form:

$$\overline{\Phi}_a|_{\bar{r}=1} - \overline{\Phi}_T|_{\bar{r}=1+\bar{t}_m} = -\frac{D_a}{P_M R}\left.\frac{d\overline{\Phi}_a}{d\bar{r}}\right|_{\bar{r}=1}. \tag{43}$$

Applying Eqs. (43) and (30) at the inner side of the microvessel wall, we get:

$$\left.\frac{d\overline{\Phi}_a}{d\bar{r}}\right|_{\bar{r}=1} = -\frac{1}{2}; \quad \overline{\Phi}_a|_{\bar{r}=1} - \overline{\Phi}_T|_{\bar{r}=1+\bar{t}_m} = \frac{D_a}{2P_M R}, \tag{44}$$

Differentiating Eq. (41) yields:

$$\frac{d\overline{\Phi}_a}{d\bar{r}} = -\bar{A}_a\left(\frac{\bar{r}^3}{4} - \frac{\bar{r}}{2}\right) + \frac{\bar{K}}{\bar{r}}. \tag{45}$$

Applying Eq. (45) at $\bar{r} = 1$ and using Eq. (44) gives:

$$\bar{K} = -\frac{\bar{A}_a}{4} - \frac{1}{2}. \tag{46}$$

Assuming an average concentration c_0 at $z = 0$ and applying a mass balance yields:

$$\begin{aligned} &c_0\int_0^R 2\pi r v\,dr - \int_0^R 2\pi r v(c_0 + \Phi - bz)dr \\ &- \pi[r_T^2 - (R + t_m)^2]zR_0 = 0. \end{aligned} \tag{47}$$

Using Eq. (34) and substituting for b in Eq. (47) gives:

$$\int_0^R 2\pi r v\Phi dr = 0. \tag{48}$$

Splitting the integral term in Eq. (48) into two terms to account for the existence of two zones yields in dimensionless form:

$$I = I_c + I_a = \int_0^\sigma \bar{r}\bar{v}\overline{\Phi}_c d\bar{r} + \int_\sigma^1 \bar{r}\bar{v}\overline{\Phi}_a d\bar{r} = 0. \tag{49}$$

Substituting for the velocity and concentration profiles in Eqs. (39)–(41), we get:

$$\begin{aligned} I_c = &\int_0^\sigma \bar{r}(\bar{A}_c\bar{r}^2 + B_1) \\ &\left[\overline{\Phi}_i + \frac{D_a}{D_c}\left(\bar{A}_c\frac{\bar{r}^4}{16} + B_2\bar{r}^2 + B_3\right)\right]d\bar{r}; \\ B_1 = &\bar{v}_i - \bar{A}_c\sigma^2; \quad B_2 = -\frac{\bar{v}_i}{4} + \bar{A}_c\frac{\sigma^2}{4}; \\ B_3 = &-\frac{3}{16}\bar{A}_c\sigma^4 + \frac{\sigma^2}{4}\bar{v}_i, \end{aligned} \tag{50}$$

$$\begin{aligned} I_a = \int_\sigma^1 \bar{r}\bar{A}_a(\bar{r}^2 - 1)\Bigg(&\overline{\Phi}_a|_{\bar{r}=1} + \bar{A}_a\left(\frac{\bar{r}^4}{16} - \frac{\bar{r}^2}{4} + \frac{3}{16}\right) \\ &+ \bar{K}\ln\bar{r}\Bigg)d\bar{r}. \end{aligned} \tag{51}$$

Integrating gives:

$$I_c = J_c + \left(\bar{A}_c\frac{\sigma^4}{4} + B_1\frac{\sigma^2}{2}\right)\overline{\Phi}_i, \tag{52}$$

$$I_a = J_a + \bar{A}_a\left(-\frac{\sigma^4}{4} + \frac{\sigma^2}{2} - \frac{1}{4}\right)\overline{\Phi}_a|_{\bar{r}=1}, \tag{53}$$

where J_c and J_a are given by:

$$\begin{aligned} \frac{D_c}{D_a}J_c = &-\bar{A}_c^2\frac{\sigma^8}{128} + \bar{A}_c\left(B_2 - \frac{B_1}{16}\right)\frac{\sigma^6}{6} \\ &+ (\bar{A}_c B_3 + B_1 B_2)\frac{\sigma^4}{4} + B_1 B_3\frac{\sigma^2}{2}, \end{aligned} \tag{54}$$

$$\frac{J_a}{\bar{A}_a} = -\bar{A}_a\left[\frac{1-\sigma^8}{128} - \frac{5(1-\sigma^6)}{96} + \frac{7(1-\sigma^4)}{64} - \frac{3(1-\sigma^2)}{32}\right] + \bar{K}\left(-\frac{\sigma^4}{4}\ln\sigma - \frac{1-\sigma^4}{16} + \frac{\sigma^2}{2}\ln\sigma + \frac{1-\sigma^2}{4}\right). \quad (55)$$

Applying Eq. (48) at the interface between the core and annular zones yields:

$$\overline{\Phi}_i - \overline{\Phi}_a|_{\bar{r}=1} = \Lambda, \quad (56)$$

where Λ is given by:

$$\Lambda = -\bar{A}_a\left(\frac{\sigma^4}{16} - \frac{\sigma^2}{4} + \frac{3}{16}\right) + \bar{K}\ln\sigma. \quad (57)$$

Combining Eqs. (49), (52), (53), and (56) yields:

$$\overline{\Phi}_a|_{\bar{r}=1} = \frac{J_c + J_a + \left(\bar{A}_c\frac{\sigma^4}{4} + B_1\frac{\sigma^2}{2}\right)\Lambda}{\bar{A}_a\left(\frac{1}{4} + \frac{\sigma^4}{4} - \frac{\sigma^2}{2}\right) - \bar{A}_c\frac{\sigma^4}{4} - B_1\frac{\sigma^2}{2}}. \quad (58)$$

Using Eq. (44) yields the following expression for the centerline value $\overline{\Phi}_c|_{\bar{r}=0}$:

$$\overline{\Phi}_c|_{\bar{r}=0} = \overline{\Phi}_i - \frac{3}{16}\frac{D_a}{D_c}\overline{A}_c\sigma^4 + \frac{D_a}{D_c}\frac{\overline{v}_i}{4}\sigma^2. \quad (59)$$

The mass transfer coefficient can be determined using:

$$k_m(c_{av} - c_a|_{r=R}) = P_M(c_a|_{r=R} - c_T|_{r=R+t_m}). \quad (60)$$

The average solute concentration in blood c_{av} is given by:

$$c_{av} = \frac{\int_0^R 2\pi r v c\,dr}{Q} = \frac{\int_0^R 2\pi r v c\,dr}{\int_0^R 2\pi r v\,dr}, \quad (61)$$

in which v and c represent v_a and c_a in the annular zone, and v_c and c_c in the core zone, respectively. Then, using Eqs. (25) and (48) yields:

$$c_{av} = c_0 - bz. \quad (62)$$

Substituting Eqs. (62) and (25) into Eq. (61) gives:

$$k_m(-\Phi_a|_{r=R}) = P_M(\Phi_a|_{r=R} - \Phi_T|_{r=R+t_m}). \quad (63)$$

Then, combining Eqs. (63) and (36) provides:

$$k_m = \frac{[r_T^2 - (R + t_m)^2]R_0}{2R(-\Phi_a|_{r=R})}. \quad (64)$$

4 Computational procedure and results

Solving the problem requires a number of steps. The dimensionless profiles $\overline{\Phi}_c$ and $\overline{\Phi}_a$ require the values of σ, the core region hematocrit, H_C, and the ratio D_a/D_c. The steps are as follows: (i) for specific values of H_T and σ, calculate the core zone hematocrit H_C, the dimensionless core zone viscosity μ_c/μ_a, the discharge hematocrit H_D, and the dimensionless blood viscosity μ_{app}/μ_a using Eqs. (10)–(13), (ii) determine $\bar{A}_a$ and $\bar{A}_c$ using Eq. (42), (iii) obtain $\bar{v}_i$, $\bar{K}$, and Λ using Eqs. (39), (46), and (56), respectively, and (iv) find B_1, B_2, B_3, $\bar{J}_c$, and $\bar{J}_a$ using Eqs. (54) and (55). Finally, Eqs. (58), (56), and (59) can be used to provide the values of $\overline{\Phi}_a|_{\bar{r}=1}$, $\overline{\Phi}_i$, and $\overline{\Phi}_c|_{\bar{r}=0}$ at the inner side of the wall, the interface between the two zones inside the microvessel, and the centerline, respectively. The use of Eq. (44) and the dimensionless value of $D_a/(P_M R)$ provides the value of $\overline{\Phi}_T|_{\bar{r}=1+\bar{t}_m}$. For H_D and microvessel diameter (2R) given, finding H_T and σ requires trial and error calculations using the blood viscosity correlation in Pries *et al.* [8].

The dimensionless profiles for $\overline{\Phi}_c$ and $\overline{\Phi}_a$ are given by Eqs. (40) and (41) as functions of r/R, and in a dimensional form by Eqs. (31), (32), and (24) for Φ_c, Φ_a, and Φ_T

Table 1: Results for $\sigma = 0.9$ and $H_T = 34.2\%$

Constant	Limiting low D_c value	Intermediate case: $D_c = D_a$	Limiting high D_c value
μ_c/μ_a	1.947	1.947	1.947
D_c/D_a	0.4771	1.000	3.192
H_C	42.2%	42.2%	42.2%
μ_{app}/μ_a	1.469	1.469	1.469
H_D	40.0%	40.0%	40.0%
$\bar{A}_a$	−2.937	−2.937	−2.937
$\bar{A}_c$	−1.509	−1.509	−1.509
$\bar{v}_i$	0.5581	0.5581	0.5581
$\bar{K}$	0.2343	0.2343	0.2343
$\overline{\Phi}_c\|_{\bar{r}=0}$	0.2993	0.1433	0.04554
$\overline{\Phi}_i$	−0.3266	−0.1553	−0.04800
$\overline{\Phi}_a\|_{\bar{r}=1}$	−0.3783	−0.2070	−0.09970
I_c	9.132×10^{-3}	4.591×10^{-3}	1.747×10^{-3}
I_a	-9.132×10^{-3}	-4.591×10^{-3}	-1.747×10^{-3}

as functions of r. The dimensionless variables are defined by Eqs. (37) and (38). The concentrations can be obtained using Eq. (25) where b, providing the rate of change of concentration in the axial direction, is given by Eq. (34). As mentioned previously, the expressions are not valid in the near vicinity of z equal to zero. The range for D_c/D_a can be obtained using Maxwell equation for two limiting cases:

$$\begin{aligned} &\text{Low } D_{RBC}/D_a: \frac{D_c}{D_a} = 2\frac{1-H_c}{2+H_c};\\ &\text{High } D_{RBC}/D_a: \frac{D_c}{D_a} = \frac{1+2H_c}{1-H_c}, \end{aligned} \tag{65}$$

and an intermediate case: $D_c/D_a = 1$. The following table provides an application of the abovementioned procedure as an example.

Table 1 shows the impact of diffusion in RBCs on the concentrations inside the microvessel, with obviously less deviations at high diffusion coefficient D_c as anticipated, as higher diffusion coefficient yields less resistance to mass transfer. The concentrations decrease with increase in r at constant z. This allows solute transport from blood to tissue. Some negative values for $\overline{\Phi}$ are expected since the profile is expected to satisfy Eq. (49). The negative values are deviations and do not represent concentrations as seen from Eq. (25). Using the analytically determined profiles and performing numerical calculations confirm that Eq. (49) is satisfied as seen from Table 1.

As an example, the model is applied to glucose transport from blood flowing in a capillary to the surrounding Krogh tissue cylinder. For the purpose of comparison, the data and values from ref. [3] are used and summarized in Table 2.

The dimensional concentration profiles are obtained from Eq. (25) as:

$$\text{at } 0 \le r \le \bar{r}_i R \quad c_c = c_0 + \phi^* \overline{\Phi}_c - bz, \tag{66}$$

$$\text{at } \bar{r}_i R \le r \le R \quad c_a = c_0 + \phi^* \overline{\Phi}_a - bz. \tag{67}$$

At the critical value z_{cr} given by:

$$\text{at } z_{cr} = \frac{c_0 + \phi^* \overline{\Phi}_T|_{r_T}}{b} \; c_T = 0. \tag{68}$$

As noticed from Figure 2, all glucose concentrations drop as z increases due to solute transport from blood to tissue, followed by diffusion and chemical reaction in the Krogh tissue surrounding the capillary. The results for the average glucose concentration in blood, c_{av} (z), and

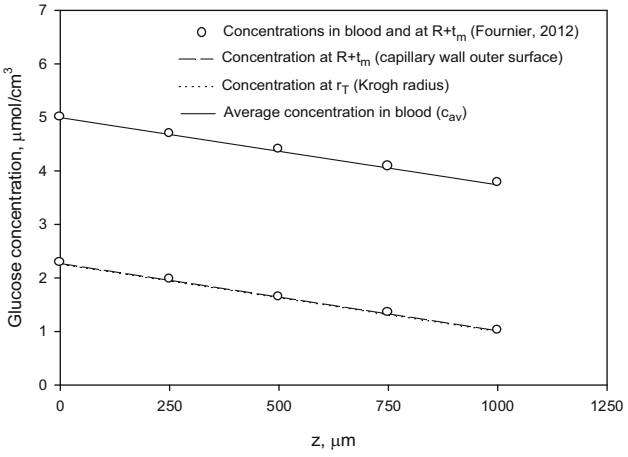

Figure 2: Compared results for the average glucose concentration in blood, and the concentrations of glucose at the outer surface of the capillary wall with published results in ref. [3]. At the Krogh cylinder radius, the concentration is very close to the concentration at the outer surface of the capillary wall as in ref. [3].

Table 2: Data used for glucose transport from blood flow in a capillary

Property	Symbol	Value	Ref. [3]
D	Diffusion coefficient in water	0.91×10^{-5} cm^2/s	p. 221
D_a	Diffusion coefficient in plasma	0.63 D	Eq. (5.60)
$2R$	Capillary diameter	10 μm	Table 5.1
v^*	Average blood velocity	0.05 cm/s	Table 5.1
t_m	Wall thickness	0.5 μm	Table 5.1
L	Length	1,000 μm	Table 5.1
R_0	Rate of glucose consumption	0.01 μmol/cm^3 s	p. 221
P_M	Membrane permeability	5.76×10^{-5} cm/s	p. 221
c_0	Average concentration at $z = 0$	5 μmol/cm^3	p. 221
a	Glucose molecular radius	0.36 nm	p. 221
D_T/D	Ratio of D_T to D	≈0.9	Figure 5.12
r_T	Krogh cylinder radius (assumed in [3])	40 μm	p. 229

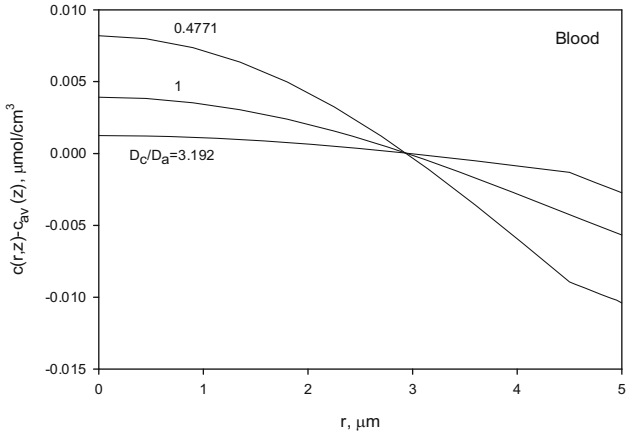

Figure 3: Profiles of the deviations of glucose concentration from the average concentration in blood for different values of D_c/D_a.

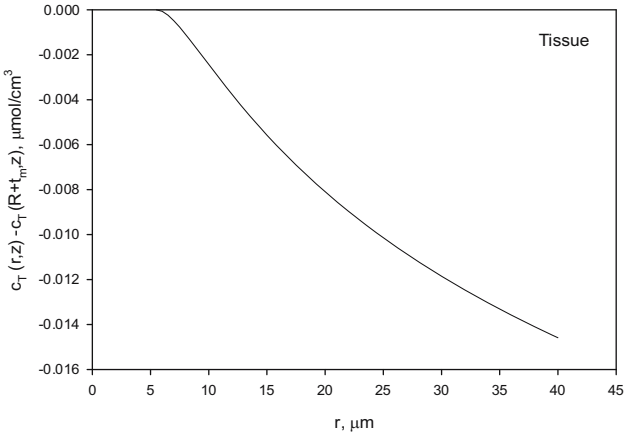

Figure 4: Profile for the drop in glucose concentration from the value of the concentration at the outer surface of the capillary wall (independent of D_c/D_a).

the glucose concentration at the outer surface of the capillary wall, $c_T(R + t_m, z)$, are both very consistent with Fournier's results. The results for the concentrations at the Krogh tissue radius, $c_T(r_T, z)$, are very close to those at the outer surface of the capillary wall as seen from Figure 2, and from Figure 5.18 in ref. [3]. The profiles for the deviations of concentration in blood from the average concentration, $c(r,z)-c_{av}(z)$, show a decrease in concentration as r gets closer to the capillary inner wall as glucose is transported from blood to tissue, with less deviations from the average concentration of glucose, at higher D_c/D_a (Figure 3). The drop in glucose concentration in the Krogh cylinder from its value at the outer surface of the wall, $c_T(r, z) - c_T(R + t_m, z)$, is plotted in Figure 4. Considering the previous results in Figures 2–4 and Table 3, we conclude that the significant change in the r-direction occurs in the membrane, as noted by Fournier [3].

The mass transfer coefficient results are reported in Table 3, showing higher values at higher D_c/D_a. Nevertheless, the significantly lower permeability P_M plays the predominant role in determining the overall mass transfer coefficient as also mentioned by Fournier [3]. The critical values z_{cr} are close in the three D_c/D_a cases (about 1.8 mm), and larger than the capillary length in Table 2.

5 Conclusion

The concentration profiles are determined based on solute conservation of mass, mass transport equations, and relevant boundary conditions. The steady state model accounts for convection-diffusion in the microvessel, transport through the microvessel membrane, and diffusion and zero-order reaction in the Krogh tissue cylinder. Velocity gradients in the microvessel are accounted for in mass transfer calculations using the marginal zone theory results in the cell-free layer and the core region where RBCs concentrate. The solution for mass transfer requires a detailed procedure starting with blood flow calculations, and ending with the determination of the concentrations at the core zone-cell-free layer interface, and both sides of the microvessel membrane. The use of the concentration values at the boundary points yields different profiles in the microvessel and in the Krogh cylinder

Table 3: Results for glucose dissolution using Tables 1 and 2

Constant	Limiting low D_c value	Intermediate case: $D_c = D_a$	Limiting high D_c value
b, µmol/cm^3 µm	1.256×10^{-3}	1.256×10^{-3}	1.256×10^{-3}
ϕ^*, µmol/cm^3	2.738×10^{-2}	2.738×10^{-2}	2.738×10^{-2}
$c_T(R + t_m,z)-c_{av}(z)$, µmol/cm^3	−2.7356	−2.7309	−2.7280
k_m, cm/s	1.516×10^{-2}	2.769×10^{-2}	5.750×10^{-2}
z_{cr}, µm	1,791	1,795	1,797

using the relevant equations discussed above. The solution excludes a small region near z equal to zero. Large Péclet number and microvessel length are required for neglecting the axial diffusional terms in the microvessel and tissue sides. The estimation of diffusion coefficients and permeability is not discussed here and can be found in Fournier [3]. The approach used here can be extended to treat different kinetic models, while accounting for Fåhraeus and Fåhraeus–Lindqvist effects in blood microvessels. The use of Maxwell equation to determine the effective diffusivity of the solute in the core region of the microvessel is not restricted to low volume fractions of the dispersed phase (RBCs in our case) as noted in ref. [36]. The model is validated against the results of Fournier [3] for the average glucose concentration in blood, and the glucose concentrations at the outer surface of the capillary wall and at the Krogh cylinder radius.

Funding information: The authors state no funding involved.

Author contributions: All authors have accepted responsibility for the entire content of this manuscript and approved its submission.

Conflict of interest: The authors state no conflict of interest.

References

[1] Fåhraeus R. The suspension stability of blood. Physiol Rev 1929;9:241–74.
[2] Fåhraeus R, Lindqvist T. The viscosity of the blood in narrow capillary tubes. Am J Physiol. 1931;96:562–8.
[3] Fournier RL. Basic transport phenomena in biomedical engineering. Boca Raton: CRC Press; 2012.
[4] Goldsmith HL, Cokelet GR, Gaehtgens P. Robin Fåhræus: evolution of his concepts in cardiovascular physiology. Am J Physiol Heart Circ Physiol. 1989;257:H1005–15.
[5] Toksvang LN, Berg RMG. Using a classic paper by Robin Fåhraeus and Torsten Lindqvist to teach basic hemorheology. Adv Physiol Educ. 2013;37:129–33.
[6] Secomb TW, Pries AR. Blood viscosity in microvessels: experiment and theory. Comptes Rendus Phys. 2013;14:470–8.
[7] Haynes RF. Physical basis of the dependence of blood viscosity on tube radius. Am J Physiol. 1960;198:1193–200.
[8] Pries AR, Neuhaus D, Gaehtgens P. Blood viscosity in tube flow: dependence on diameter and hematocrit. Am J Physiol Heart Circ Phys. 1992;263:H1770–8.
[9] Sharan M, Popel AS. A two-phase model for flow of blood in narrow tubes with increased effective viscosity near the wall. Biorheology. 2001;38:415–28.
[10] Sriram K, Intaglietta M, Tartakovsky DM. Non-Newtonian flow of blood in arterioles: consequences for wall shear stress measurements. Microcirculation. 2014;21(7):628–39.
[11] Chebbi R. Dynamics of blood flow: modeling of the Fåhræus–Lindqvist effect. J Biol Phys. 2015;41(3):313–26.
[12] Weert KV. Numerical and experimental analysis of shear-induced migration in suspension flow. (A thesis for the degree of Master). Eindhoven, Netherlands: Eindhoven University; 2005.
[13] Mansour MH, Bressloff NW, Shearman CP. Red blood cell migration in microvessels. Biorheology. 2010;47:73–93.
[14] Chebbi R., Dynamics of blood flow: modeling of Fåhraeus and Fåhraeus-Lindqvist effects using a shear-induced red blood cell migration model. J Biol Phys. 2018;44:591–603.
[15] Chebbi R. A two-zone shear-induced red blood cell migration model for blood flow in microvessels. Front Phys. 2019;7:206.
[16] Leighton DT, Acrivos A. The shear-induced migration of particles in concentrated suspension. J Fluid Mech. 1987;181:415–39.
[17] Phillips RJ, Armstrong RC, Brown RA. A constitutive equation for concentrated suspensions that accounts for shear-induced particle migration. Phys Fluids. 1992;4:30–40.
[18] Moyers-Gonzalez M, Owens RG, Fang J. A non-homogeneous constitutive model for human blood. Part 1. Model derivation and steady flow. J Fluid Mech. 2008;617:327–54.
[19] Moyers-Gonzalez MA, Owens RG. Mathematical modelling of the cell-depleted peripheral layer in the steady flow of blood in a tube. Biorheology. 2010;47(1):39–71.
[20] Dimakopoulos Y, Kelesidis G, Tsouka S, Georgiou GC, Tsamopoulos J. Hemodynamics in stenotic vessels of small diameter under steady state conditions: Effect of visco-elasticity and migration of red blood cells. Biorheology. 2015;52(3):183–210.
[21] Mavrantzas VG, Beris AN. Modelling the rheology and the flow-induced concentration changes in polymer solutions. Phys Rev Lett. 1992;69:273–6. Errata. 1993;70,2659.
[22] Tsouka S, Dimakopoulos Y, Mavrantzas V, Tsamopoulos J. Stress-gradient induced migration of polymers in corrugated channels. J Rheol. 2014;58(4):911–47.
[23] Arciero JC, Causin P, Malgaroli F. Mathematical methods for modeling the microcirculation. AIMS Biophys. 2017;4:362–99.
[24] Bessonov N, Sequeira A, Simakov S, Vassilevski Yu, Volpert V. Methods of blood flow modelling. Math Model Nat Phenom. 2016;11:1–25.
[25] Krogh A. The number and distribution of capillaries in muscles with calculations of the oxygen pressure head necessary for supplying the tissue. J Physiol. 1919;52:409–15.
[26] Popel AS. Theory of oxygen transport to tissue. Crit Rev Biomed Eng. 1989;17:257–321.
[27] Goldman D. Theoretical models of microvascular oxygen transport to tissue. Microcirculation 2008;15:795–811.
[28] Truskey GA, Yuan F, Katz DF. Transport phenomena in biological systems. New Jersey: Pearson; 2010.
[29] Hellums JD. The resistance to oxygen transport in the capillaries relative to that in the surrounding tissue. Microvasc Res. 1977;13:131–6.
[30] Groebe K. An easy-to-use model for O_2 supply to red muscle. Validity of assumptions, sensitivity to errors in data. Biophys J. 1995;68:1246–69.

[31] Federspiel WJ, Popel AS. A theoretical analysis of the effect of the particulate nature of blood on oxygen release in capillaries. Microvasc Res. 1986;32:164–89.
[32] Eggleton CD, Vadapalli A, Roy TK, Popel AS. Calculations of intracapillary oxygen tension distributions in muscle. Math Biosci. 2000;167:123–43.
[33] Vadapalli A, Goldman D, Popel AS. Calculations of oxygen transport by red blood cells and hemoglobin solutions in capillaries. Artif Cell Blood Substit Immobil Biotechnol. 2002;30:157–88.
[34] Lucker A, Weber B, Jenny PA. Dynamic model of oxygen transport from capillaries to tissue with moving red blood cells. Am J Physiol Heart Circ Physiol. 2015;308:H206–H216.
[35] Dinarvand S, Rashidi MM, Doosthoseini A. Analytical approximate solutions for two-dimensional viscous flow through expanding or contracting gaps with permeable walls. Cent Eur J Phys. 2009;7(4):791–9.
[36] Bird RB, Stewart WE, Lightfoot EN. Transport phenomena. New York: Wiley; 2007.